The Astrophysical Journal, 812:42 (14pp), 2015 October 10 doi:10.1088/0004-637X/812/1/42

STARSPOT DISTRIBUTIONS ON FULLY CONVECTIVE M DWARFS: IMPLICATIONS FOR RADIAL VELOCITY PLANET SEARCHES

J. R. Barnes[1], S. V. Jeffers[2], H. R. A. Jones[3], Ya. V. Pavlenko[3,4], J. S. Jenkins[4,5], C. A. Haswell[1], and M. E. Lohr[1]
[1] Department of Physical Sciences, The Open University, Walton Hall, Milton Keynes MK7 6AA, UK; john.barnes@open.ac.uk
[2] Institut für Astrophysik, Georg-August-Universität, Friedrich-Hund-Platz 1, D-37077 Gttingen, Germany
[3] Centre for Astrophysics Research, University of Hertfordshire, College Lane, Hatfield AL10 9AB, UK
[4] Main Astronomical Observatory of the National Academy of Sciences of Ukraine, Golosiiv Woods, Kyiv-127, 03680, Ukraine
[5] Departamento de Astronomía, Universidad de Chile, Camino del Observatorio 1515, Las Condes, Santiago, Chile
Received 2015 February 13; accepted 2015 August 26; published 2015 October 7

ABSTRACT

Since M4.5–M9 dwarfs exhibit equatorial rotation velocities of the order of 10 km s^{-1} on average, radial velocity surveys targeting this stellar population will likely need to find methods to effectively remove starspot jitter. We present the first high resolution Doppler images of the M4.5 dwarf, GJ 791.2A, and the M9 dwarf, LP 944-20. The time series spectra of both objects reveal numerous line profile distortions over the rotation period of each star, which we interpret as starspots. The transient distortions are modeled with spot/photosphere contrast ratios that correspond to model atmosphere temperature differences of $T_{\rm phot} - T_{\rm spot} = 300$ and 200 K. GJ 791.2A is a fully convective star with $v \sin i = 35.1$ km s^{-1}. Although we find more starspot structure at high latitudes, we reconstruct spots at a range of phases and latitudes with a mean spot filling of ∼3%. LP 944-20 is one of the brightest known late-M dwarfs, with spectral type M9V and $v \sin i = 30.8$ km s^{-1}. Its spectral time series exhibits two dominant transient line distortions that are reconstructed as high latitude spots, while a mean spot filling factor of only 1.5% is found. The occurrence of low-contrast spots at predominantly high latitudes, which we see in both targets here, is, in general, likely to be responsible for the low amplitude photometric variability seen in late-M dwarfs. For GJ 791.2A, the radial velocities induced by the starspot features yield an rms velocity variability of 138 m s^{-1}, which can be reduced by a factor of 1.9 using our reconstructed surface brightness distributions.

Key words: methods: data analysis – planets and satellites: detection – stars: individual (GJ 791.2A, LP 944-20) – stars: late-type – starspots – techniques: spectroscopic

1. INTRODUCTION

The *Kepler* mission has yielded many transiting planet candidates (Borucki et al. 2011; Batalha et al. 2013) while ground based radial velocity (RV) surveys at red or infrared wavelengths (Bean et al. 2010; Barnes et al. 2012) have now demonstrated precision in late-M stars of ∼2.5 m s^{-1} (Barnes et al. 2014) indicating the potential to detect rocky planets down to $M \sim 1.5\ M_{\oplus}$. For early-M stars, planet occurrence fractions of the order of 0.5 (Bonfils et al. 2013) and even >1 per star (Tuomi et al. 2014) are expected, so understanding any limitations from stellar variability is vital. Meanwhile, M dwarf planet hosting stars have been found to exhibit significant activity with a photometric variability of up to ∼10% (Crossfield et al. 2011; Knutson et al. 2011). Activity will limit searches for low-mass planets around low-mass stars in a reasonable number of epochs (Barnes et al. 2011) because by M4.5V stars, on average, become moderate rotators (Jenkins et al. 2009), with mean $v \sin i \sim 5$ km s^{-1}, while rotation is even greater (∼15 km s) for the latest-M stars despite a decline in Hα activity (Mohanty & Basri 2003; Reiners & Basri 2010).

Our understanding of magnetic field generation in fully convective stars has only seen advances in relatively recent times. Reiners & Basri (2007) first observed strong magnetic fields in fully convective stars from Stokes *I* measurements of FeH lines. A further study (Reiners & Basri 2009) found that only 14% of the total magnetic flux detected in Stokes *I* is seen in Stokes *V*. Because Stokes *I* sees the total magnetic field and Stokes *V* only sees the net magnetic field, this implies that most of the field is arranged on small scales over which opposite polarities cancel each other out. The net field in early M dwarfs, which still possess radiative cores, is nevertheless even lower, at only 6%. This implies that fully convective stars possess more ordered dipolar field structure in agreement with the Stokes *V* Zeeman Doppler imaging studies of Donati et al. (2008) and Morin et al. (2008a, 2010). Donati et al. and Morin et al. found that the topology among the earliest M stars (M0V–M3V) was dominantly toroidal with non-axisymmetric poloidal field structures, while the mid-M (M4V) stars at the fully convective transition boundary exhibited axisymmetric large-scale poloidal fields. The latest stars in the sample (M5–M8V) were found to possess either strongly axisymmetric dipolar fields or weak fields with a significant non-axisymmetric component. The stars in these studies did not, however, possess sufficient rotation to enable brightness imaging.

Applying Doppler imaging techniques to rapidly rotating M1–M2 dwarfs, Barnes & Collier Cameron (2001) and Barnes et al. (2004) have shown that early-M dwarfs are more uniformly covered with spots than F, G, and K stars. Images of two M4V dwarfs, however, reveal fewer spots and low spot filling factors (Morin et al. 2008b; Phan-Bao et al. 2009). While Crossfield et al. (2014) have published a cloud map of the cool brown dwarf, Luhmen 16B, no images of late M dwarfs have been published thus far. In this paper, we present Doppler images of the latest fully convective M dwarfs, using spectral time series observations at red-optical wavelengths.

1.1. GJ 791.2A

GJ 791.2A is an M4.5 dwarf with a previously estimated $v \sin i = 32.1 \pm 1.7$ kms^{-1} (Delfosse et al. 1998). At 8.84 pc, it is a bright, nearby binary system with an astrometrically

Table 1
System Parameters and Summary of Observations for GJ 791.2A and LP 944-20

		GJ 791.2A	LP 944-20
Spectral Type	⋯	M4.5V	M9V
$v \sin i$	(km s^{-1})	35.1 ± 0.4	30.8 ± 0.5
Axial inclination	(deg)	54 ± 9	55 ± 9
Rotation Period	(days)	0.3088 ± 0.0058	0.162 ± 0.005
R_* (derived)	($R_\odot$)	0.265 ± 0.035	0.120 ± 0.014
R_* (estimated)[a]	($R_\odot$)	0.279 ± 0.028	0.118 ± 0.012
N_{obs}	⋯	111	39
Exposure times	(s)	180	360
Observation span	(MJD)	56904.13046	⋯
2014 Sep 03	⋯	−56904.15523	⋯
Observation span	(MJD)	56906.98665	56907.22626
2014 Sep 06	⋯	−56907.21841	−56907.40070

Note.
[a] Baraffe et al. (1998) assuming 320 Myr (LP 944-20) and 600 Myr (GJ 791.2A) ages.

determined period of 1.4731 ± 0.0008 years, a maximum separation of ∼0.″16 and primary component mass of 0.286 $M_\odot$ (Benedict et al. 2000). Our spectra do not show evidence for the secondary 0.126 $M_\odot$ component, which is estimated to be $\Delta V = 3.23$ fainter than the primary component. Montes et al. (2001) found that this young disk system does not satisfy Hyades Supercluster membership.

1.2. LP 944-20

Flaring radio emission has been detected on the M9 dwarf LP 944-20 (Berger et al. 2001), which nevertheless exhibits low L_{H_α}/L_{bol}, despite a $v \sin i = 30$ km s^{-1} (Mohanty & Basri 2003). Ribas (2003) determined that LP 944-20 may be a member of the Castor moving group (day = 5–20 pc from the Sun) with an implied age of 320 ± 80 Myr. Dieterich et al. (2014) report a parallax of 155.89 ± 1.03 mas (day = 6.41 ± 0.04 pc).

2. OBSERVATIONS

We used the Ultraviolet and Visual Echelle Spectrograph (UVES) at the Very Large Telescope (VLT) to obtain time series spectra of both stars, with a central wavelength of 8300 Å, and a spectral range of 6437–10253 Å. Observations were made with a 0.″4 slit, yielding a spectral resolution of ∼90,000. We observed GJ 791.2A on 2014 September 3 and 6. Since pointing restrictions were in place for the first half of the first night, only 11 spectra of GJ 791.2A were taken, spanning 0.595 hr (35.7 minutes), before telescope closure due to high winds. Both GJ 791.2A and LP 944-20 were observed on September 6 for 5.562 hr and 4.187 hr, respectively. Observations are summarized in Table 1.

The spectra were optimally extracted (Horne 1986) using the Starlink package, ECHOMOP, which removes all but the strongest sky lines. Error information based on photon statistics and readout noise is propagated throughout the extraction process.

3. DOPPLER IMAGING

3.1. Least Squares Deconvolution

To enable starspot induced line distortions to be detected for imaging purposes, we applied our implementation of least squares deconvolution (Barnes et al. 1998). Using this procedure, a high signal-to-noise ratio (S/N) mean line profile is derived for each spectrum with the effects of blending due to rotationally broadened lines removed. The deconvolution algorithm and analysis applied to M dwarfs is detailed in Barnes et al. (2014). We have used high S/N observations of non-rotating stars of the same or similar spectral type to derive empirical line lists for deconvolution. For GJ 791.2A, we used GJ 105B (M4.5V) as a slowly rotating standard star, while for LP 944-20, LP 888-18 (M7.5V) was used.

Obtaining an empirical line list involves removing the blaze, normalizing and stitching into a one-dimensional spectrum. Normalization of spectra is carried out by fitting a spline or polynomial to the spectrum. The minimum number of spline knots or polynomial degree to fit the continuum behavior is adopted and generally varies with the length of the spectrum being fitted. By rejecting outliers at a specified level below each fit and iteratively re-fitting, a good approximation to the continuum level can generally be found. For stars such as M dwarfs, which contain so many lines that only a pseudo-continuum is seen, we found that it was necessary to obtain the maximum value of the spectrum in 10 Å intervals and use these values for continuum fitting.

Line wavelengths and depths are then identified empirically, with normalized depths >0.1. Lines with strong chromospheric components such as Hα and the infrared Na doublet and Ca II triplet are removed. Although LP888-18 has been used successfully to recover precise radial velocities in M7–M9V stars (Barnes et al. 2014), a closer spectral type match for LP 944-20 would likely enable line profiles with more optimal S/Ns to be obtained. Line lists from model atmospheres do not provide a precise enough match to the observed spectra to enable deconvolution, although in Section 3.3 we use models to obtain line equivalent width ratios and intensity ratios for Doppler imaging. By determining line lists empirically, we include not only atomic lines, but also molecular lines, which are the dominant sources of opacity in cooler atmospheres. For instance, the Vienna Line Database (Piskunov et al. 1995; Kupka et al. 1999; Ryabchikova et al. 2011) contains ∼15,800 lines with normalized depths of 0.5–1.0 in the 6500–10250 Å range for the coolest available temperature of $T = 3500$ K. The database currently holds a limited number of molecular species; however, for $T = 3500$ K, ∼95% of the opacities are due to TiO and MgH (comprising 92% and 3%, respectively). Of the remaining 5% of atomic metal lines, half have normalized line depths <0.165. By 3000 K, spectral energy distributions continue to be dominated by TiO and other diatomic molecular bands, particularly CaH, VO, CrH, and FeH (Pavlenko 2014; Pavlenko & Schmidt 2015). We estimate that 99% of opacities are due to molecules at $T = 3000$ K, which falls to 60% by $T = 2300$ K for atmospheres with 10%–20% dust. The validity of using temperature sensitive molecular lines for Doppler imaging is investigated in detail in Section 3.3.

For GJ 791.2A, the mean S/N of our input spectra was 57.5. With 7939 lines in the 6485–10253 Å region, the deconvolved profiles possess a mean wavelength of $\bar{\lambda} = 7781$ Å and a mean

S/N of 3600; an improvement of ∼63 in S/N. Similarly, for LP 944-20 the input and output S/Ns were 18.9 and 584, respectively. With little flux in the bluest orders, we used the spectral range 8417–10253 Å ($\bar{\lambda}$ = 9033 Å), which contains 4150 lines, enabling an effective S/N improvement of ∼31 with deconvolution. During deconvolution, telluric lines were used to correct for drifts in UVES following procedures detailed in Barnes et al. (2014).

3.2. Image Reconstruction Algorithm

We used the program DoTS (Collier Cameron 2001) to recover Doppler images of our targets. DoTS uses a model with two brightness levels to derive images from high resolution, high cadence time series spectra. A spot filling factor, f_i, is derived for each pixel, i, on the model star by iteratively fitting the time series spectra.

Since there are generally more image pixels than data points, and the data possesses finite S/N, often with phase gaps, no unique image can fit the data for a given level of χ^2. A regularizing function is therefore imposed on the image. DoTS uses the image entropy

$$S(f) = -\sum_{i=1}^{n} w_i \left[f_i \ln \frac{f_i}{m} + (1 - f_i) \ln \frac{1 - f_i}{1 - m} \right] \quad (1)$$

which has the effect of minimizing spurious correlations between image pixels. The function, $S(f)$, combines the entropy, $f \ln f$, of both the spot image, f, and the image $(1 - f) \ln (1 - f)$ of the clean photosphere. The default model m is the value that a pixel will assume in the absence of any other constraint imposed by the data. Full details of the image recovery procedure are given in (Collier Cameron 2001).

To obtain an image solution, the image pixels, f_i are adjusted iteratively to maximize the function

$$Q(f) = S(f) - \lambda \chi^2(f) \quad (2)$$

where λ is the Lagrange multiplier. The value of the Lagrange multiplier is determined such that the image solution lies on the surface with $\chi^2 \simeq M$, where M is the number of measurements in the data set. In practice, systematics, or either underestimated or overestimated data uncertainties mean that the ideal level of χ^2 is not achieved. The point at which the rate of change of χ^2 with each iteration shows a marked decrease indicates a suitable stopping point. Continuing iterations can lead to spot features being recovered that are not justified by the data. A fixed number of iterations is generally adopted for a given data set, which means that the optimal parameters will then provide the best fit (as determined by the minimum achieved χ^2) to the data.

3.3. Input Models for Imaging

A study of *G*, *R*, and *I* photometric variability in M dwarfs was made by Rockenfeller et al. (2006) for late M dwarfs. While dust clouds were ruled out for the M9 star 2M1707+64, the light curves were best fit by a dusty atmosphere with cool spots and $\Delta T = 100\ K$. Berdyugina (2005) has also shown that $T_{\rm phot} - T_{\rm spot}$ declines with decreasing $T_{\rm phot}$ in giants, leading us to expect contrasts corresponding to temperature differences of only a few hundred K in mid–late M dwarfs. Doppler images of V374 Peg (M4V) were obtained by Morin et al. (2008b) who employed least squares deconvolution using only atomic line lists and a blackbody temperature difference of $\Delta T = T_{\rm phot} - T_{\rm spot} = 400$ K.

Since Doppler imaging requires S/Ns of a few hundred to identify starspots in time series spectra and derive reliable images, we combined the signal from as many lines as possible in our observed spectra, including both atomic and molecular lines. Since the behavior of such a combination of lines with different temperature sensitivities is not clear, we investigated the validity of using least squares deconvolved mean line profiles for Doppler imaging of cool M dwarf atmospheres.

Synthetic spectra were computed using the BT-Settl model atmospheres (Allard et al. 2012) by the WITA code, first described in Gadun & Pavlenko (1997) using opacity sources listed in Pavlenko et al. (2007). Further details can also be found in Pavlenko (2014) and Pavlenko & Schmidt (2015). High resolution disk integrated model spectra were generated in the 2000–3200 K interval in steps of 100 K. In addition, spectra were generated for limb-angles, $\mu = \cos(\theta) = 0.1, 0.2, 0.4, 0.6, 0.8$ *and* 1.0, where θ is the limb-angle measured from disk center. The spectra were interpolated onto our observation wavelengths to enable us to determine the contrast ratios and line equivalent width behavior as a function of limb angle over the wavelengths used for deconvolution. For GJ 791.2A, we adopted $T_{\rm phot} = 3000$ K and for LP 944-20, we adopted $T_{\rm phot} = 2300$ K in accordance with Reid & Hawley (2005; see also Kaltenegger & Traub 2009).

In the case of GJ 791.2A, we carried out deconvolution on the synthetic spectra for $T = 2600$–3000 K (at 100 K intervals) over the same wavelength range as described in Section 3.1, but using a model-derived line list for the disk integrated spectrum with $T = 3000$ K. Deconvolution was performed for the spectra at each μ and the equivalent width of the deconvolved line was measured. We adopted the four-parameter limb-darkening equation used by Claret (2000) to fit the line equivalent width variability as a function of limb angle. In addition, we determined the mean intensity of the model spectra at each μ over the deconvolution wavelengths and again fit the same four-parameter equation to obtain the center-to-limb variation in intensity. We carried out exactly the same procedure for LP 944-20, using a model deconvolution line list for $T = 2300$ K to deconvolve spectra at all μ for $T = 2000$–2300 K.

Figure 1 illustrates the behavior of the line equivalent width and intensity as a function of limb-angle, μ. The equivalent width at disk center ($\mu = 1.0$) increases monotonically as the temperature decreases from 3000 to 2600 K. This behavior is the result of the line opacities becoming stronger at cooler temperatures. By 2500 K (not shown), the equivalent width begins to decrease again with a relative value of 1.28 (compared to 1.26 for 2700 K and 1.31 for 2600 K). For the cooler temperature range, with a deconvolution template of 2300 K (Figure 1, top right panel), a monotonic decrease in equivalent width at limb center is instead seen. This behavior occurs because the line opacities are so numerous and strong that the lines are effectively weakened relative to the pseudo-continuum level. The equivalent width decreases with decreasing limb-angle, except for $T = 3000$ K, which shows a slight increase out to $\mu = 0.5$ (Figure 1, top left). Nevertheless, at the cooler temperatures (Figure 1, top right) this trend reverses at the smallest limb angles for

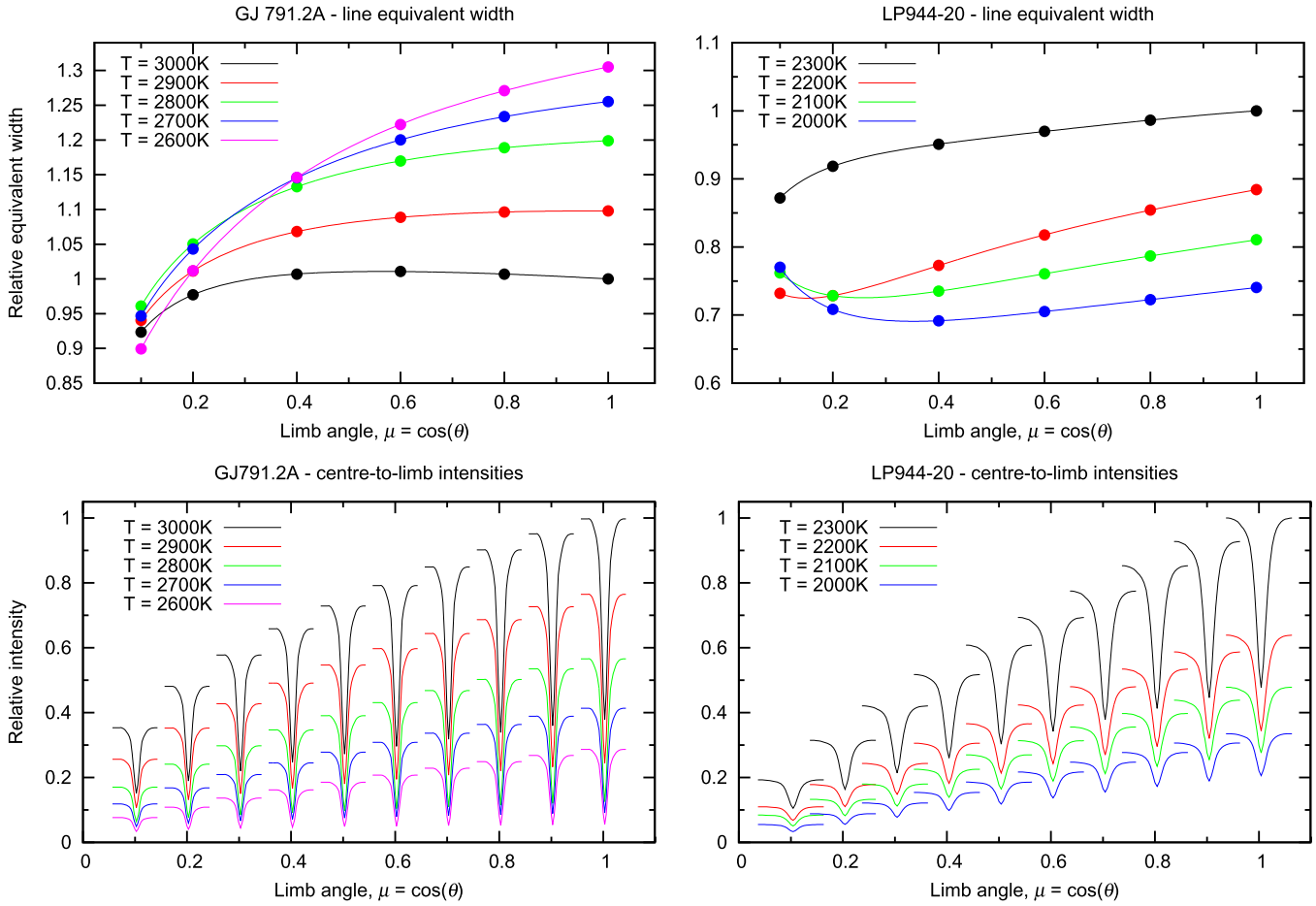

Figure 1. Top: the deconvolved equivalent width as a function of limb-angle, μ, for BT Settl spectra computed with the WITA code (see Section 3.3 for details). For GJ 791.2A (left), all spectra were deconvolved using a line list with $T = 3000$ K and for LP 944-20 (right), using a line list with $T = 2300$ K. Bottom: the center-to-limb local intensity profiles obtained from deconvolved synthetic spectra. The line profiles are derived from our standard stars, GJ105 (M4.5V) and LP 888-18 (M7.5V). The center-to-limb variation of profile equivalent width in the upper panels is adopted. The intensities at each limb-angle, obtained from the synthetic spectra, are the mean intensities determined over the appropriate deconvolution wavelength ranges for our target stars.

T = 2000–2200 K. While decreases in line equivalent width may result from real changes in line depths, a mismatch between the line list and the spectrum to which deconvolution is applied will lead to non-optimal recovery of the line profile. This effect thus also contributes to trends of the recovered line equivalent width with limb angle and temperature.

The relative center-to-limb variability is illustrated in the lower panels of Figure 1. The intensities at each temperature are relative to the central intensity of the 3000 K spectrum (Figure 1, bottom left) and the 2300 K spectrum (Figure 1, bottom right). The line profiles plotted in Figure 1 and used for image recovery are, however, derived from the same slowly rotating standards used in Section 3.1 rather than the model spectra, following Morin et al. (2008b). Because the standard stars are observed with the same instrumental setup, and because individual line opacities are not a good match, as noted in Section 3.1, we expect that they better represent the local intensity profile *shapes* than those derived from the models. The equivalent width from the template star derived line profile is thus adopted for the imagining procedure while the relative equivalent width between the photosphere and spot is obtained from the models (i.e., as indicated in the upper panels of Figure 1).

For a star with a photospheric temperature of $T_{\rm phot}$ = 3000 K, the line core is very close to the continuum level at $T_{\rm spot}$ = 2700 K, being either above or below depending on the limb angle. Hence, it is likely that spot features will only be distinguishable (in terms of contrast) if the temperature difference between the photosphere and spot possess $\Delta T \gtrsim 300$ K. This corresponds to a contrast at disk center of $I^c_{\rm spot}/I^c_{\rm phot} = 0.41$ for the adopted models with $T_{\rm phot} = 3000$ K. With smaller temperature differences ($\Delta T < 300$ K), we expect that the contrast will be too small to enable the spot induced distortions to be adequately fit with spot filling factors $\leqslant$1.0. Similarly, for a star with $T_{\rm phot} = 2300\,K$, a temperature difference of $\Delta T \sim 200$ K ($I^c_{\rm spot}/I^c_{\rm phot} = 0.48$) is likely required to enable spot filling factors of 1.0. In Section 4, we present results for image recovery using spot/temperature contrasts corresponding to $\Delta T = 300$ K and $\Delta T = 200$ K for GJ 791.2A and LP 944-20, respectively, and additionally investigate the effect of modifying the adopted contrasts.

3.4. Rotation Periods and System Parameters

The SuperWASP archive (Butters et al. 2010)[6] contains 10,166 observations of GJ 791.2A, with mean photometric errors of 0.24, spanning ~6.5 years. SuperWASP is, however,

[6] http://www.superwasp.org

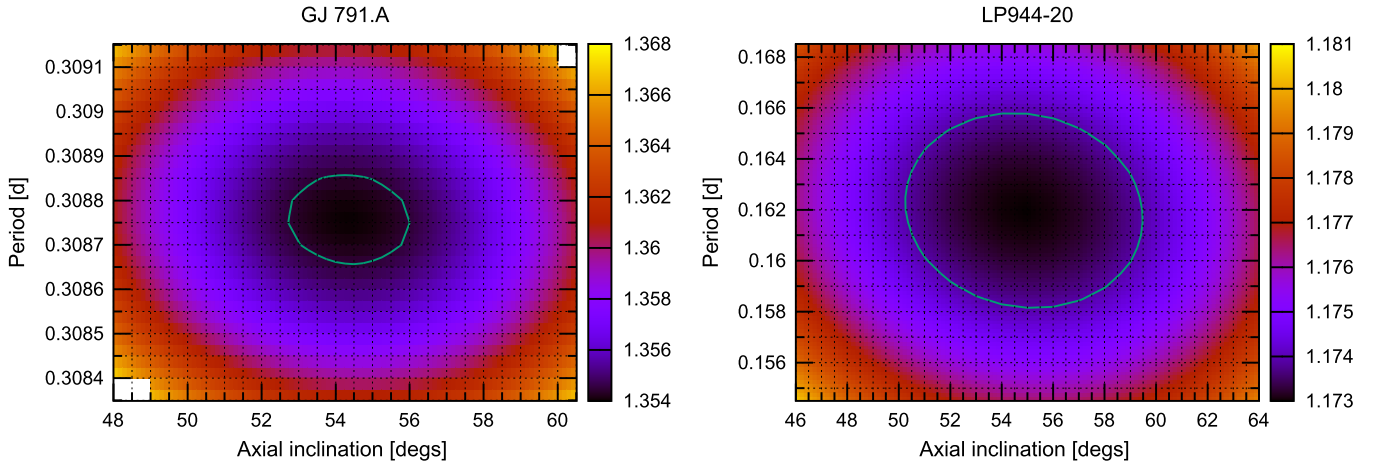

Figure 2. Reduced χ^2 (χ^2_r) plots of rotation period, P, vs. axial inclination, i with 67.3% confidence level. $\chi^2_{r\min} = 1.354$ (GJ 791.2A) and $\chi^2_{r\min} = 1.173$ (LP 944-20). The derived parameters and uncertainties are listed in Table 1.

not sensitive to objects, such as LP 944-20, with $V \gtrsim 15.0$. We searched for periodicity in the data using a phase dispersion minimization algorithm (Lohr et al. 2014), obtaining $P = 0.257025(1)$ day. The amplitude of variability, $\Delta V = 0.02$(8% of the photometric errors), is comparable with the amplitudes found by Rockenfeller et al. (2006) for other variable M dwarfs. However, folding subsets of data spanning only a few tens of days does not reveal obvious periodicity, suggesting that higher cadence data with better photometric precision is needed.

Adopting published parameters can lead to systematic and characteristic biases in the reconstructed images (Rice et al. 1989; Unruh & Collier Cameron 1995). For example, the rotation velocity, $v \sin i$, and line profile depth combination are correlated, and the optimal χ^2 for a given input model must be determined (Barnes et al. 2000). Over-estimation of profile equivalent width typically leads to images with completely filled polar regions as the fitting procedure attempts to match the observed profiles by reducing the depth of the line center. This can be seen, for example, in the images of G dwarfs presented by Barnes et al. (1998), as compared with the same images in Barnes et al. (2001), where a lower equivalent width and $v \sin i$ were adopted following a revised parameter optimization procedure, which we use here. The main system parameters, recovered by minimizing χ^2 in the multi-dimensional parameter space are listed in Table 1.

Uncertainties in parameters can be obtained from the likelihood function based on the minimum χ^2 values obtained and the number of data points contributing to the image solution, as outlined in Section 3.2. We have also considered the effect of systematic errors that could arise from adopting the wrong local intensity profiles and the ΔT values and limb darkening parameters investigated in Section 4. For both GJ 791.2A and LP 944-20, using the model-derived local intensity profiles leads to $v \sin i$ values that are $0.2\,\mathrm{km\,s^{-1}}$ lower than with the adopted standard star local intensity profiles for instance. These additional sources of systematic error are included in our error estimates in Table 1, indicating $v \sin i$ uncertainties of $\sim 0.5\,\mathrm{km\,s^{-1}}$ and inclination uncertainties of the order of 10°. Morin et al. (2008b) similarly estimated $v \sin i$ uncertainties of $\sim 1\,\mathrm{km\,s^{-1}}$ for the M4V star, V374 Peg.

The axial rotation period

$$P = \frac{2\pi R_* \sin i}{v \sin i} \tag{3}$$

can be reliably determined by utilizing repeated starspot distortions in the line profiles for $\gtrsim 1$ stellar rotation. We assumed uncertainties of 10% for the estimated radii of GJ 791.2A and LP 944-20 in Table 1, which are in agreement with the discrepancies between theoretical and observed M dwarf radii (Stassun et al. 2012; Williams et al. 2015). Although GJ 791.2A is considered a young disk object, which was not found to be a member of the Hyades supercluster by Montes et al. (2001), we have assumed a radius appropriate for a 600 Myr object following Baraffe et al. (1998). Our radius uncertainty of 10% corresponds to a minimum age of 100 Myr. At 3 Gyr, Baraffe et al. (1998) estimate a radius that is <2% larger at 600 Gyr, which is somewhat lower than our adopted 10% uncertainty. From the estimated radii (Baraffe et al. 1998) in Table 1, we find maximum periods for our targets of $P_{\mathrm{estimated}}/\sin i = 0.4023 \pm 0.0406$ day and 0.1939 ± 0.0200 day respectively. Using DoTS, we then performed χ^2 minimization searches for P versus i (for $P < P_{\mathrm{estimated}}$), which yielded $P = 0.3088$ day and $i = 54°$ for GJ 791.2A. Similarly, for LP 944-20 $P = 0.1620$ day and $i = 55°$ (Figure 2). The fact that periodicities can be determined this way indicates the coherence of spots on a single rotation timescale for LP 944-20 and on three day timescales for GJ 791.2A. We note that the SuperWASP period of 0.257 days leads to a significantly poorer fit to the data with a mis-match of repeated starspot features. The derived radii for both stars are consistent with the estimated model radii with 10% uncertainties.

4. RESULTS

The observed time series deconvolved profiles, along with the regularized fits using the parameters in Table 1 are shown for both stars in Figure 3. To enhance the appearance of starspots, the time series profiles are shown as 2D colorscale plots divided by the mean profile in Figure 4 for GJ 791.2A and Figure 5 for LP 944-20. Figures 4 and 5 also show the fits with the mean profile removed along with the residual time series.

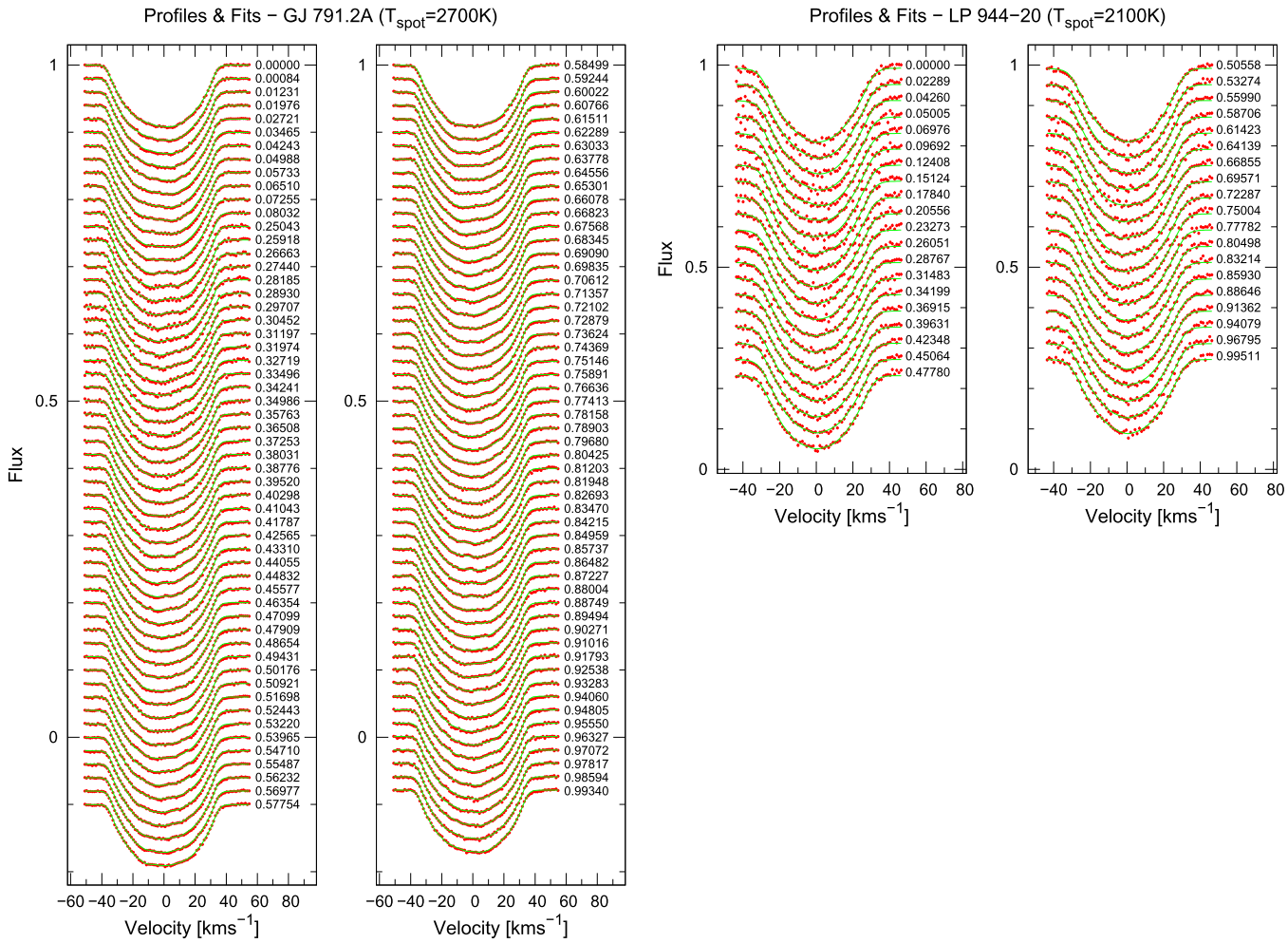

Figure 3. Deconvolved profiles for GJ 791.2A (left) and LP 944-20 (right). The data are plotted as points along with the error bars. The maximum entropy regularized profiles corresponding to the images in Figures 6 and 8 are shown as line plots. Observations are phased with epochs HJD0 = 2456904.63601 (GJ 791.2A) and HJD0 = 2456907.73034 (LP 944-20), which are the mid-exposures of the first observation in each time series.

The reconstructed maps in Figures 6–8, which have 2° pixel resolution, reveal spots reconstructed at a range of latitudes. The gradient of a starspot feature in the time series spectra determines the stellar latitude at which it is reconstructed, while the recovered phase is given by the time at which the feature crosses the profile center. The right hand panels in Figures 6–8 indicate the mean spot filling at each latitude, while the mean spot filling as a function of phase is shown for different latitude ranges in the panels below each Mercator projection. The 3D images at rotation phases 0.00, 0.25, 0.50, and 0.75 are also shown for all cases.

4.1. GJ 791.2A

GJ 791.2A shows a number of starspot features of different sizes distributed across most phases. We used $T_{\rm phot} = 3000$ K and $T_{\rm spot} = 2700$ K, with a disk center contrast ratio of $I^c_{\rm spot}/I^c_{\rm phot} = 0.41$ for the image reconstruction in Figure 6. The phase range $\phi = 0.0000$–0.0803 is provided by observations on September 3 that align spot features with those from September 6, which first come into view at phases $\phi \sim 0.8$–1.0. Phase overlap between nights is confined to the narrow $\phi = 0.0000$–0.0008 range, corresponding to the first observation on September 3 and the last observation on September 6. Any starspots at the center of the 0.0803–0.2504 phase gap in observations are still seen for 66% of the total time they are physically visible on the star. Spots in the phase gap can thus be reconstructed, albeit with potentially decreased reliability in latitude.

Since $\cos(\theta) \propto$ starspot trail gradient to first order (where θ is the stellar latitude), and $\cos(\theta)$ is a slowly changing function when θ is small, the elongation of spots at low latitudes is a reflection of the uncertainty in θ. There are ∼17.5 resolution elements in the rotationally broadened profile of GJ 791.2A, equivalent to ∼10°.3 resolution, or 0.029 in phase, at the equator (the 180 s exposures result in rotational blurring of only 2°.2). The weakest low latitude features appear elongated with FWHM values of $\Delta\phi \sim 4°$–$6°$and $\Delta\theta \sim 22°$–$30°$. These features are approximately equivalent to circular spots with radii ∼9°.5–13°.5.

The maximum spot filling factor in the image of GJ 791.2A is $f_{\rm max} = 0.823$ (82.3%) and the mean spot filling is $\bar{f} = 0.032$ (3.2%). Spot activity is seen at all latitudes, but with peak filling factors concentrated at $\theta = 59°$ and particularly $\theta = 75°$ as indicated in Figure 6 (panel to right of Mercator map). Spot coverage as a function of phase (Figure 6, panel below Mercator map) is higher on average in the 45°–90° region (dashed line) compared with the lower −30°−45° region (dotted line), again demonstrating the greater

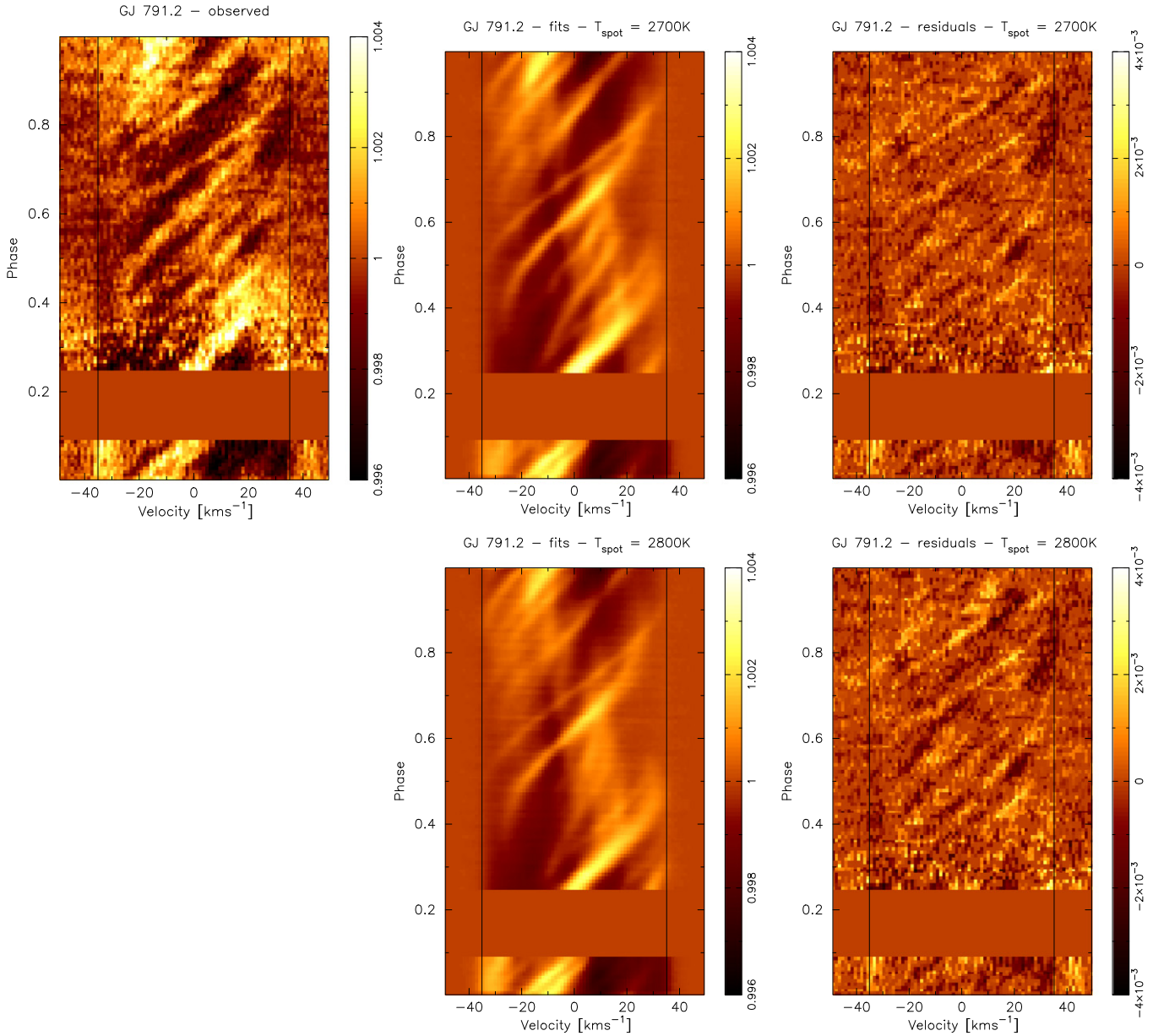

Figure 4. Mean profile divided deconvolved line profile time series (left), fits (middle), and fit residuals (right) for GJ 791.2A using a spot temperature of $T_{\rm spot} = 2700$ K (upper panels) and $T_{\rm spot} = 2800$ K (lower panels). The starspot features appear as white trails while black trails are regions that are more negative relative to the mean profile. The spectra are centered on the observed rest frame and phased according to the adopted 0.3088 day period of GJ 791.2A. The vertical lines indicate a $v \sin i$ profile width of 35.1 km s^{-1}.

degree of spot filling at higher latitudes. To some extent this is due to the fact that the number of resolution elements is greater at lower latitudes where features are better resolved. In other words, in the $-30°$–$45°$ range, the spot coverage as a function of phase approaches zero in regions outside the spots, which can be seen to produce more narrow peaks than for the 45°–90° region.

4.1.1. Images with ΔT = 200 and 400 K

We also attempted to fit our spectra with $T_{\rm spot} = 2800$ K ($\Delta T = 200$ K) with an intensity contrast ratio at disk center of $I^c_{\rm spot}/I^c_{\rm phot} = 0.57$. However, for $T_{\rm spot} = 2800$ K, we achieved a reduced χ^2 of $\chi^2_r = 2.39$, whereas with $T_{\rm spot} = 2700$ K, we achieved $\chi^2_r = 1.35$. The contrast in the corresponding fits is lower in Figure 4 (lower panels) with noticeably greater residuals. The upper panels in Figure 7 show the image for $T_{\rm spot}$= 2800 K which shows a maximum spot filling of $f_{\rm max} = 0.983$ and a mean spot filling of $\bar{f} = 0.038$. The image is very similar to the $T_{\rm spot} = 2700$ K image, except for the greater degree of spot filling. As expected, DoTS has tried to account for the lack of contrast by enlarging some of the spots (e.g., the spot at phase 0.62 and $-30°$) in an attempt to fit the starspot distortions in the line profiles.

With $T_{\rm spot} = 2600$ K ($\Delta T = 400$ K), we find a contrast of $I^c_{\rm spot}/I^c_{\rm phot} = 0.29$. The reconstructed image closely resembles the $\Delta T = 300$ K image, but shows reduced spot filling factors of $f_{\rm max} = 0.690$ and a mean spot filling of $\bar{f} = 0.026$ (χ^2_r= 1.38).

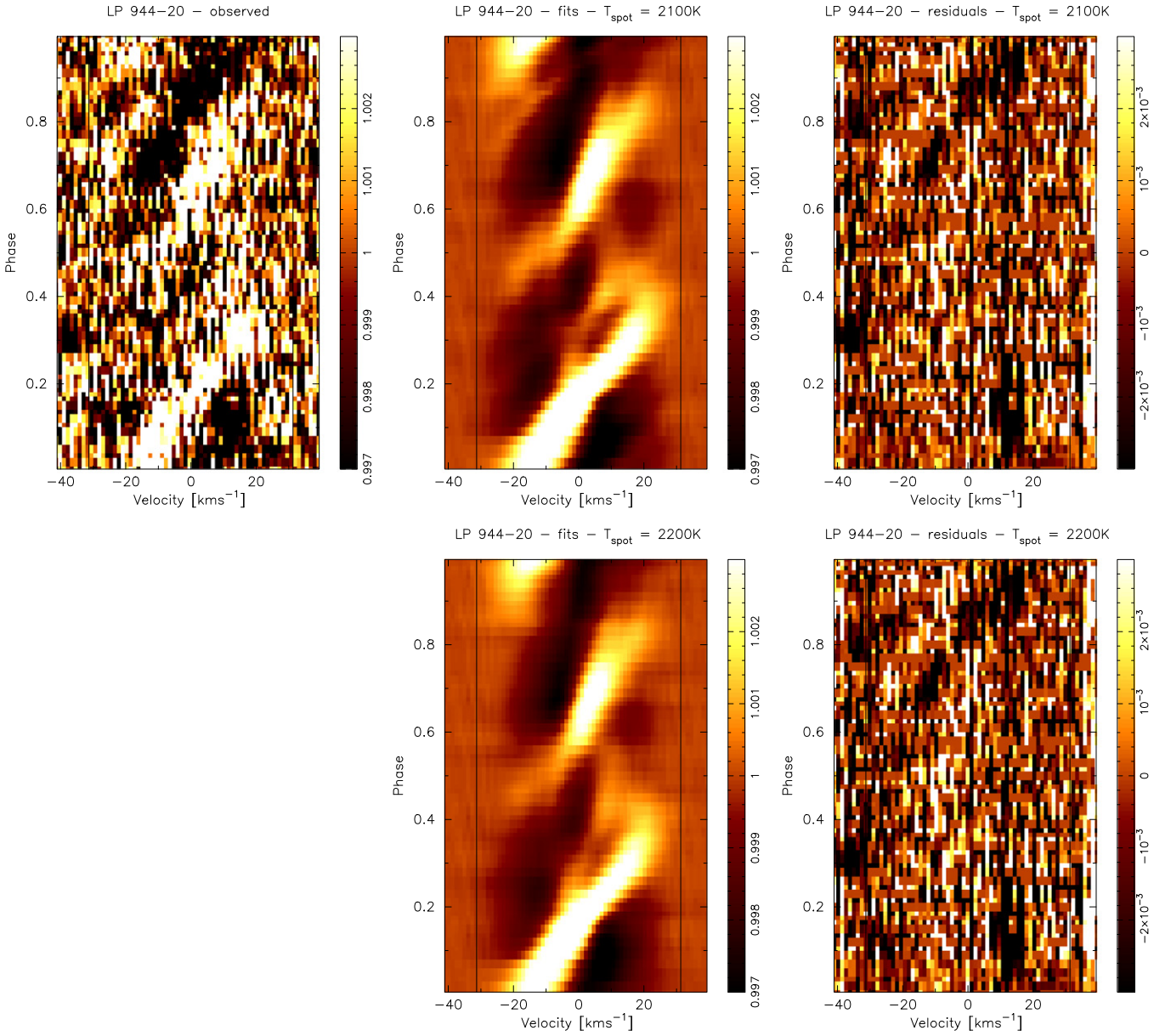

Figure 5. Same as for Figure 4, but for LP 944-20.

4.2. The Effect of Limb Darkening Uncertainty on Image Reconstruction

The concentration of spots seen on GJ 791.2A in Figure 6 at 75° appear to occur in a relatively narrow band, which is most evident in the 3D plots shown below the Mercator projection in Figure 6. Features that do not traverse the whole $v \sin i$ extent of the star are reconstructed at high latitudes. Closely separated starspot trails (in phase), or broader, more complex trails cannot be resolved and can result in the merging of starspot features in the images. At higher latitudes, this can lead to the appearance of arcs or rings of structure. To further investigate the axisymmetric structure at 75° on GJ 791.2A, we have explored a number of different input models.

Overestimating the degree of limb darkening leads to a more V-shaped line profile, requiring a higher $v \sin i$ to fit the time series spectra. On the other hand, a lower degree of limb darkening leads to a more U-shaped profile and a typically lower $v \sin i$ estimate, potentially reducing circumpolar structure. To assess the reality of the high latitude axisymmetric structure on GJ 791.2A, we investigated the effect of modifying the limb darkening in our input models. We scaled the center-to-limb intensities at each limb-angle using a linear relationship, such that $I_{\rm adjusted} = I_{\rm model}(1 - \xi(1 - \mu))$, where ξ is the scale factor. We investigated $\xi = -0.2$, -0.1, 0.1, and 0.2 and found that the χ^2 after fitting our profiles was minimized by reducing the limb darkening by 10% (i.e., $\xi = -0.1$). A reduced $\chi^2_r = 1.18$ was achieved compared with $\chi^2_r = 1.35$ for the default case. The resulting image is shown in Figure 7 (lower panels), which shows that the axisymmetric ring at high latitude structure is less prominent. Mean and maximum spot filling factors of $\bar{f} = 0.033$ and $f_{\rm max} = 0.76$ are found.

With a 20% reduction in limb darkening, the high latitude axisymmetric ring structure is reduced in prominence, leaving only the main concentrations of spots, but all lower latitude structure becomes confined to the latitude range

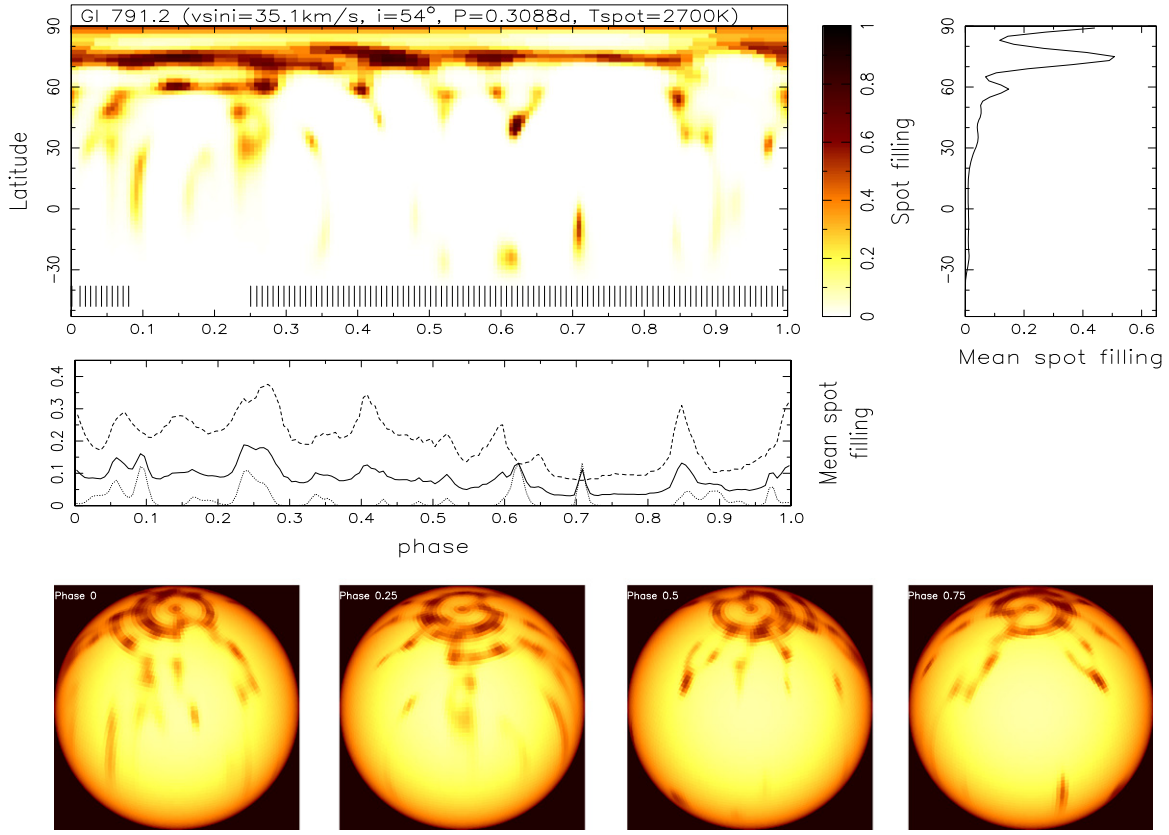

Figure 6. Maximum entropy regularized image reconstructions of GJ 791.2A plotted as Mercator (top) and 3D projections (bottom). The image of GJ 791.2A is shown for parameters optimized with $T_{\rm phot} = 3000$ K and $T_{\rm spot} = 2700$ K, which have a contrast ratio at the disk center of $I_{\rm spot}(0)/I_{\rm phot}(0) = 0.41$. The tick marks in the Mercator plot indicate the phases of observation. The latitudinal mean spot filling is shown in the upper left panel. The mean phase spot filling is indicated in the panel below the Mercator map for latitudes −30°–90° (solid line), −30°–45° (dotted line), and 45°–90° (dashed line).

0°–50° ($\chi^2_r = 1.38$ is achieved). Increasing the degree of limb darkening led to strong polar filling factors and poorer fits. We also investigated using $T_{\rm phot} = 3100$ K with $\Delta T = 400$ K (a contrast ratio of $I^c_{\rm spot}/I^c_{\rm phot} = 0.45$). In this case, the center-to-limb intensity variation was similar to our optimal limb darkening (i.e., when reduced by 10%) for $T_{\rm phot} = 3000$ K. The center-to-limb trend is, however, more linear and leads to an augmentation of the axisymmetric ring compared with the image in Figure 6 with a reduced $\chi^2_r = 2.04$.

Finally, removing the center-to-limb line equivalent width variation had little discernible effect on the image, though the strength of the spot filling at 75° increased by 9%. Optimizing the center-to-limb variation in intensity and the nonlinearity of the limb darkening is thus important for ensuring that artefacts are minimized. The need to reduce the limb darkening by 10% gives an empirical indication of the systematic uncertainty in the current models for cool M dwarfs.

4.3. LP 944-20

The two dominant starspot trails seen in the time series spectra of LP 944-20 (Figure 5) possess steep gradients, leading us to expect that starspots should be reconstructed at predominantly high latitudes. The image of LP 944-20 in Figure 8 (top two panels) is reconstructed with $i = 55°$ and $P = 0.1620$ days and shows that activity is concentrated in two groups at $\phi \sim 0.2$ and 0.65, approximately half a rotation phase apart. For $v \sin i = 30.8\,{\rm km\,s^{-1}}$, the equatorial spot resolution is 11°.5. As with GJ 791.2A, spots are found at high latitude, with a maximum in the azimuthally averaged spot filling at 79°. The spot reconstructed at $\phi = 0.16$ and $\theta = 55°$ is predominantly responsible for the mean latitude filling peak at $\theta = 55°$. Given the lower S/N of the data, the smaller, weaker spots at $\phi = 0.65$, $\theta = 55°$ and $\phi = 0.925$, $\theta = 35°$ may be artefacts in the reconstruction. We also note that if lower latitude spots of similar size to those seen on GJ 791.2A are present on LP 944-20, they may not be recovered owing to the lower S/N of the data. LP 944-20 reveals a very low mean spot filling factor of $\bar{f} = 0.015$ (1.5%) for the image reconstructed with $T_{\rm phot} = 2300$ K and $T_{\rm spot} = 2100$ K ($\Delta T = 200$ K), corresponding to a contrast ratio at disk center, $I^c_{\rm spot}/I^c_{\rm phot} = 0.48$. A maximum spot filling factor, $f_{\rm max} = 0.766$ (76.6%), is found and we achieve $\chi^2_r = 1.17$.

4.3.1. LP 944-20 Image with $\Delta T = 100$ K

The image reconstruction with $T_{\rm spot} = 2200$ K ($\Delta T = 100$ K, $I^c_{\rm spot}/I^c_{\rm phot} = 0.64$) is shown in Figure 8 (bottom two panels). As with GJ 791.2A, when we investigated a reduced contrast, we found that the data are not fit so well ($\chi^2_r = 1.22$) compared with $T_{\rm spot} = 2100$ K, and that features are reconstructed with larger areas to account for the lower contrast ratio. As expected, the mean and maximum spot filling values are higher than for ($\Delta T = 200$ K), with $\bar{f} = 0.017$ and $f_{\rm max} = 0.866$. The lower S/N of the LP 944-20 time series makes the investigation of limb darkening modification more difficult. However, we found that even for $\xi = 0.2$ (20% *increase* in limb darkening), a $\chi^2_r = 1.17$ is

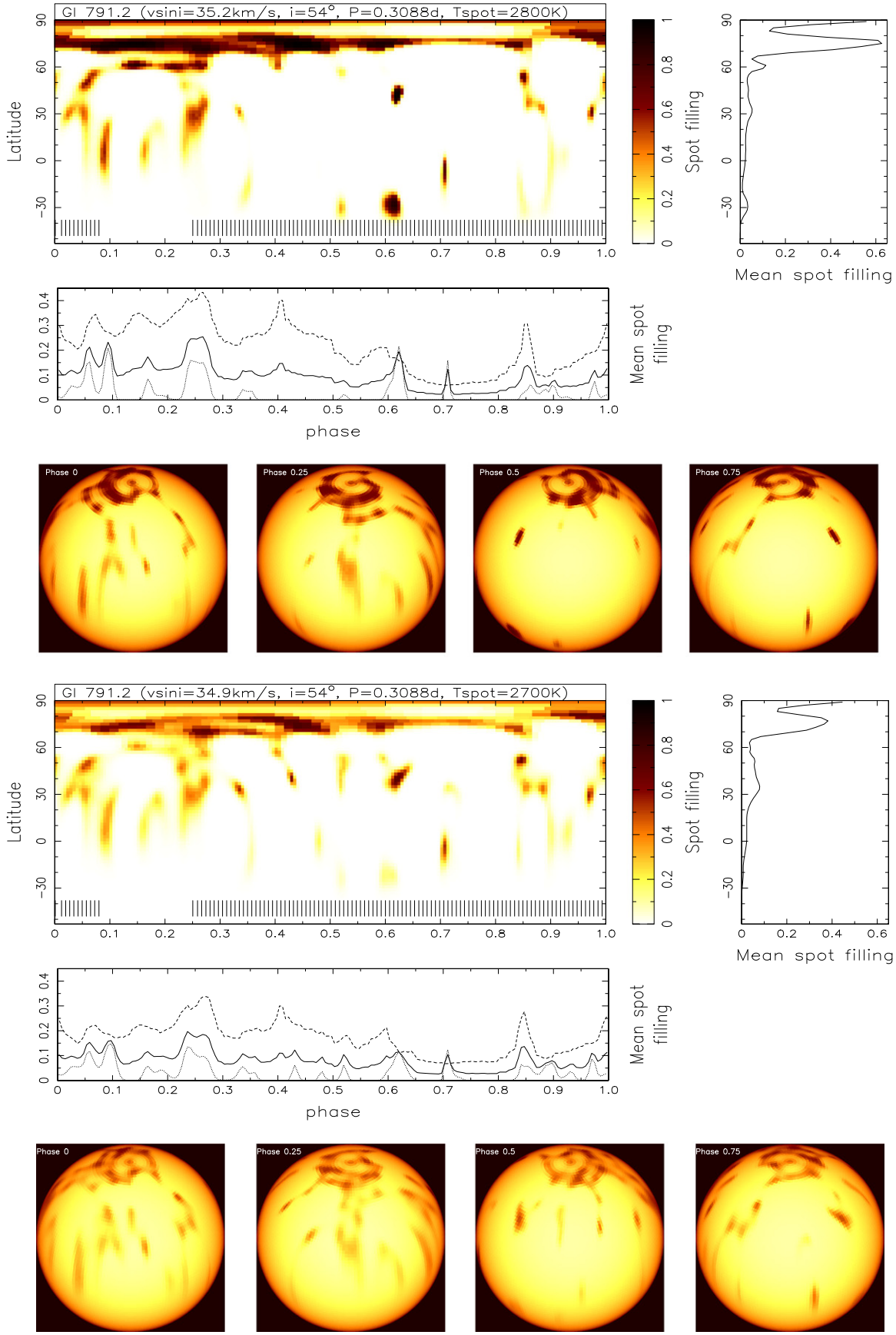

Figure 7. Same as in Figure 6 for $T_{\rm spot} = 2800$ K (top), $T_{\rm spot} = 2700$ K (bottom) with limb darkening reduced by 10% with a linear center-to-limb scaling (bottom).

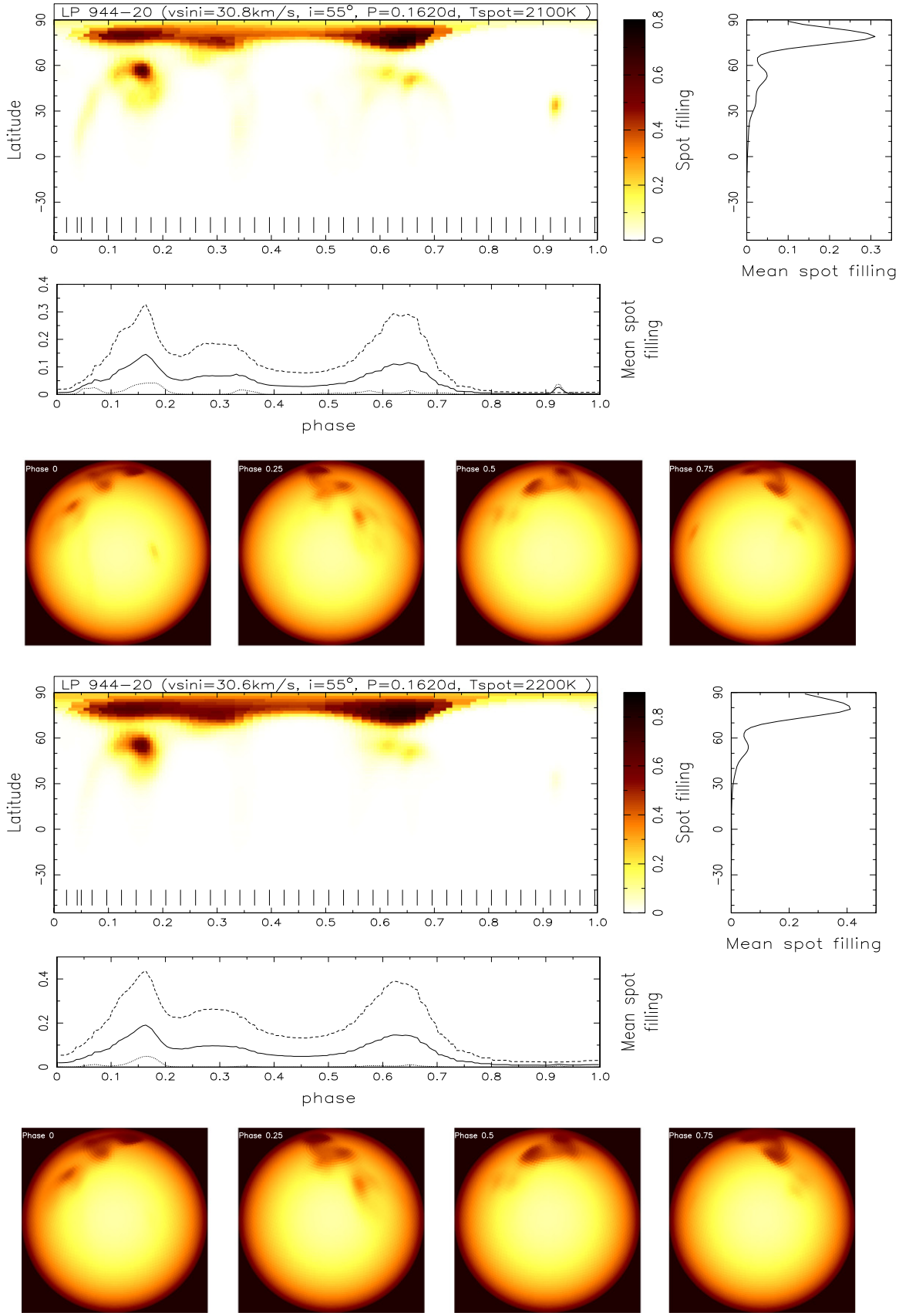

Figure 8. Maximum entropy regularized image reconstructions of LP 944-20 with panels as indicated in Figure 6. Images are shown for $T_{\rm phot} = 2300$ K, with $T_{\rm spot} = 2100$ K (upper panels) and $T_{\rm spot} = 2200$ K (lower panels), with respective contrast ratios of $I_{\rm spot}(0)/I_{\rm phot}(0) = 0.48$ and 0.64.

achieved. The image shows the same features as for our default $\Delta T = 200$ K, but with enhanced circum-polar filling, as might be expected by increasing the limb darkening ($\bar{f} = 0.019$, $f_{\max} = 0.88$).

5. RV VARIABILITY

We have cross-correlated the observed time series to determine the RV variability induced by the spots on both targets. We find a semi-amplitude of $K_* = 160\,\mathrm{m\,s^{-1}}$ for GJ 791.2A, with a corresponding RV rms of $138\,\mathrm{m\,s^{-1}}$. We also cross-correlated the time series line profile fits for $\Delta T = 300$ K. By subtracting the RVs derived from the fits from those measured for the data, following Donati et al. (2014), the starspot induced RV variability in the data can be partially corrected. We find that the RV rms can be reduced by a factor of 1.75, from $138\,\mathrm{m\,s^{-1}}$ to $79\,\mathrm{m\,s^{-1}}$. Using the optimized fits with $\Delta T = 300$ K and the limb darkening reduced by 10%, we find that the RV rms is reduced by a factor of 1.9, to $73\,\mathrm{m\,s^{-1}}$. For LP 944-20, the S/N is not sufficient to discern regular RV variability. The RV rms of $194\,\mathrm{m\,s^{-1}}$ is thus likely to be noise dominated. The regularized fits however yield an RV rms value of $93\,\mathrm{m\,s^{-1}}$.

Barnes et al. (2011) found similar RV rms values to those found here for GJ 791.2A and LP 944-20 for their scaled solar starspot model with $v \sin i = 20$–$50\,\mathrm{km\,s^{-1}}$. However, models with large spot filling fractions of either $f = 0.30$ and greater spot-to-photosphere contrast than that found here (up to $T_{\rm phot}/T_{\rm spot} = 0.65$) or models with $f = 0.62$ and similar contrast ($\Delta T = 250$ K) are required to obtain rms RVs of the order of $100\,\mathrm{m\,s^{-1}}$. Based on the evidence presented here, it thus appears that spots or spot groups are larger or more localized than the random scaled solar spots models of Barnes et al. (2011).

6. DISCUSSION

The time series spectra and Doppler images of the two mid-late M dwarfs studied here reveal significant spot structure, even at spectral type M9V. The results are in general agreement with the finding that the fall-off in fractional Hα flux in late M dwarfs (Mohanty & Basri 2003) is not in fact accompanied by a drop-off in magnetic flux (Reiners & Basri 2007), and provide further evidence for magnetic activity in the lowest mass M dwarfs. The image of GJ 791.2A shows starspots located at a range of latitudes and longitudes, but preferentially at mid to high latitudes, whereas activity is confined solely to high latitudes on LP 944-20. Late-F and early-G dwarfs, show a still greater degree of spot filling at high latitudes compared with lower latitudes, with activity confined to localized regions in phase at lower latitude (e.g., Barnes et al. 2001; Marsden et al. 2006). In contrast, Doppler images of the M1–2V stars, HK Aqr and EY Dra (Barnes & Collier Cameron 2001; Barnes et al. 2004), showed distributed activity, while differences are also seen when compared with images of the M4V stars V394 Peg (Morin et al. 2008b) and G164-31 (Phan-Bao et al. 2009), which possess similar $v \sin i$ values ($36.5\,\mathrm{km\,s^{-1}}$ and $41\,\mathrm{km\,s^{-1}}$ respectively). Morin et al. found weak features concentrated at mid latitudes with only 2% mean spot occupancy, similar to, but slightly lower than the 3.3% we find for the optimized image of GJ 791.2A. Phan-Bao et al., on the other hand, found only a weak de-centered polar spot with no low-latitude features on G164-31. The current evidence from Doppler images thus suggests that the lower photometric variability in cooler M dwarfs is the result of both lower spot contrast and more distributed activity at predominantly higher latitudes.

Zeeman Doppler imaging does not reveal the field strength in the largest spots, which show significant spot/photosphere contrast, because the amplitude of the Stokes V signature is generally small. Comparing magnetic maps and brightness maps is often difficult as a result, and because Stokes V only sees the *net* magnetic field, thus making it sensitive to field structure on larger scales. Large-scale poloidal fields were inferred for V394 Peg (Morin et al. 2008b) and G164-31 Phan-Bao et al. (2009), in agreement with the results for more slowly rotating fully convective stars (Morin et al. 2008a). Both of these stars showed only positive magnetic polarity in one hemisphere. These studies show contradictory results when the magnetic and brightness images are compared, since V394 Peg possessed multiple low to intermediate latitude features, and no polar features, while G164-31 showed only a single weak circum-polar feature. This probably suggests that even for M4V stars, the spot/photosphere contrast ratios are sufficient to preclude the detection of Stokes V signatures in the spots, meaning that magnetic and brightness maps indeed probe magnetic activity on different scales.

Our images show a number of polar or circum-polar spots, especially in GJ 791.2A that might reasonably be expected to possess a mixture of magnetic polarities. This is interesting because the degree to which the polarities cancel will likely determine the large scale global field structure, which in fully convective mid-M stars is generally axisymmetric and poloidal (Morin et al. 2008a, 2008b; Phan-Bao et al. 2009). Although we have already noted that spots recovered in brightness images do not generally correlate with magnetic field structure recovered from Stokes V, the lower contrasts in GJ 791.2A and LP 944-20, with only $T_{\rm phot} - T_{\rm spot} = 200$–$300$ K ($I^c_{\rm spot}/I^c_{\rm phot} \sim 0.4$–$0.5$), may enable at least some of the field in the spots to be more readily seen in Stokes V. This will also depend on the mixing and degree of polarity cancelling on relatively small scales and the resolution limitations of any observations.

With low contrast spots, future Stokes V observations of M dwarfs may provide the means to make more direct comparisons between spot and magnetic field morphologies and to determine why the fraction of magnetic flux seen in Stokes V compared with Stokes I is greater than for early-M spectral types (Reiners & Basri 2009). In particular, infrared polarimetric observations may offer the potential to observe the magnetic field inside starspots since the contrast ratio between spots and the photosphere is smaller at longer wavelengths. We also note that Hallinan et al. (2015) have suggested a transition from coronal activity to auroral activity in late-M stars and have suggested that such activity arises from circumpolar latitudes on the M8.5V, LSR J1835. It is not clear whether the high latitude, low contrast cool spots recovered in LP 944-20 could be related to, or contradict this mechanism.

Dedicated RV surveys such as the Habitable Zone Planet Finder (Mahadevan et al. 2010), CARMENES (Quirrenbach et al. 2010), and SPIRou (Thibault et al. 2012) will search for low-mass planets around M dwarfs. Consequently, the direct influence of magnetic activity on stellar lines is of significant importance. For stars rotating with $v \sin i = 20\,\mathrm{km\,s^{-1}}$, Barnes et al. (2011) found that $5\,M_\oplus$–$20\,M_\oplus$ habitable zone planets could be detected around $0.1\,M_\odot$, M6V stars, but would require

300 and 40 epochs, respectively. Planets with $1M_{\oplus}$ could nevertheless be detected with ∼100 epochs for stars with $v \sin i = 5\,\mathrm{km\,s^{-1}}$ and ($T_{\mathrm{phot}} - T_{\mathrm{spot}} = 250$ K). These estimates will likely be modified by the findings presented here, since we find that spot groups are more localized and larger (especially in the case of LP 944-20) than the spots modeled by Barnes et al. (2011).

Martín et al. (2006) have searched for RV variability in LP 944-20. In the optical, 15 observations spanning 841 days, with similar instrumental setups to the observations presented herein, yielded a semi-amplitude variability of $3.5\,\mathrm{km\,s^{-1}}$. By contrast, Keck/NIRSPEC observations spanning only six nights yielded a dispersion of $360\,\mathrm{m\,s^{-1}}$; an order of magnitude smaller than at optical wavelengths. Our finding of $194\,\mathrm{m\,s^{-1}}$ RV rms is thus closer in magnitude to the NIRSPEC observations. Significant spot-coverage evolution, as evidenced through other activity indicators in M dwarfs (Gomes da Silva et al. 2011), is thus likely to have biased the results of Martín et al. (2006). Given the observed activity in M dwarfs, it is clear that searches for low-mass planets will benefit from techniques that can effectively reduce or remove the substantial RV noise. Although one might not routinely expect to observe stars with rotation velocities of the order of $30\,\mathrm{km\,s^{-1}}$, the fact that Doppler imaging can be used to mitigate the effects of spots on GJ 791.2A by a factor of ∼2, indicates that it may also be a useful method for slower rotators. This is particularly important in mid–late M stars, since they show equatorial rotation velocities of $\sim 10\,\mathrm{km\,s^{-1}}$ on average (Jenkins et al. 2009). Observing only the slowest rotators is likely to bias the sample to low axial inclinations, for which it would be much more difficult to detect orbiting planets.

7. SUMMARY

Significant starspot activity is seen on M stars at the bottom of the main sequence, albeit at lower contrast compared to G and K dwarfs. Using model atmospheres as input for our image reconstructions, we find that $\Delta T \gtrsim 300$ K (contrast at disk center, $I^c_{\mathrm{spot}}/I^c_{\mathrm{phot}} = 0.41$) is required to model spots on the M4.5V, GJ 791.2A, whereas the data can be fit with $\Delta T = 100$–200 K (contrast at disk center, $I^c_{\mathrm{spot}}/I^c_{\mathrm{phot}} =$ 0.64–0.48 for the M9V LP 944-20, albeit with a marginally better fit for $\Delta T = 200$ K. The factor of two lower spot filling for LP 944-20 ($f = 0.015$) compared with GJ 791.2A ($f = 0.033$) suggests a decline in magnetic activity by M9V, as seen from other magnetic activity indicators (Mohanty & Basri 2003). However, Doppler imaging at optical wavelengths is extremely challenging for even the brightest M9V targets and it is possible that smaller, low latitude features have not been recovered on LP 944-20, owing to the lower S/N of the data. Our ability to reconstruct small-scale brightness features at all latitudes should benefit from the next generation of instruments offering higher throughput and optical (Zerbi et al. 2014) to near-infrared wavelength coverage in conjunction with near-infrared polarimetric measurements.

We are grateful to the referee for providing careful and thorough feedback during this work. We thank Prof. Ansgar Reiners for helpful discussion during this project. J.R.B., C.A.H., and M.E.L. were supported by the STFC under the grant ST/L000776/1. S.V.J. acknowledges research funding by the Deutsche Forschungsgemeinschaft (DFG) under grant SFB 963/1, project A16. J.S.J. acknowledges funding by Fondecyt through grant 3110004 and partial support from CATA-Basal (PB06, Conicyt), the GEMINI-CONICYT FUND and from the Comité Mixto ESO-GOBIERNO DE CHILE.

REFERENCES

Allard, F., Homeier, D., Freytag, B., & Sharp, C. M. 2012, in EAS Publications Ser. 57, Low-Mass Stars and the Transition Stars/Brown Dwarfs ed. C. Reylé, C. Charbonnel & M. Schultheis (Les Ulis: EDP Sciences), 3
Baraffe, I., Chabrier, G., Allard, F., & Hauschildt, P. H. 1998, A&A, 337, 403
Barnes, J. R., & Collier Cameron, A. 2001, MNRAS, 326, 950
Barnes, J. R., Collier Cameron, A., James, D. J., & Donati, J.-F. 2000, MNRAS, 314, 162
Barnes, J. R., Collier Cameron, A., James, D. J., & Steeghs, D. 2001, MNRAS, 326, 1057
Barnes, J. R., Collier Cameron, A., Unruh, Y. C., Donati, J. F., & Hussain, G. A. J. 1998, MNRAS, 299, 904
Barnes, J. R., James, D. J., & Cameron, A. C. 2004, MNRAS, 352, 589
Barnes, J. R., Jeffers, S. V., & Jones, H. R. A. 2011, MNRAS, 412, 1599
Barnes, J. R., Jenkins, J. S., Jones, H. R. A., et al. 2012, MNRAS, 424, 591
Barnes, J. R., Jenkins, J. S., Jones, H. R. A., et al. 2014, MNRAS, 439, 3094
Batalha, N. M., Rowe, J. F., Bryson, S. T., et al. 2013, ApJS, 204, 24
Bean, J. L., Seifahrt, A., Hartman, H., et al. 2010, ApJ, 713, 410
Benedict, G. F., McArthur, B. E., Franz, O. G., Wasserman, L. H., & Henry, T. J. 2000, AJ, 120, 1106
Berdyugina, S. V. 2005, LRSP, 2, 8
Berger, E., Ball, S., Becker, K. M., et al. 2001, Natur, 410, 338, #198, 891
Bonfils, X., Delfosse, X., Udry, S., et al. 2013, A&A, 549, A109
Borucki, W. J., Koch, D. G., Basri, G., et al. 2011, ApJ, 736, 19
Butters, O. W., West, R. G., Anderson, D. R., et al. 2010, A&A, 520, L10
Claret, A. 2000, A&A, 363, 1081
Collier Cameron, A. 2001, Astrotomography—Indirect Imaging Methods in Observational Astronomy, ed. H. M. J. Boffin, D. Steeghs & J. Cuypers (Berlin: Springer), 183
Crossfield, I. J. M., Barman, T., & Hansen, B. M. S. 2011, ApJ, 736, 132
Crossfield, I. J. M., Biller, B., Schlieder, J. E., et al. 2014, Natur, 505, 654
Delfosse, X., Forveille, T., Perrier, C., & Mayor, M. 1998, A&A, 331, 581
Dieterich, S. B., Henry, T. J., Jao, W.-C., et al. 2014, AJ, 147, 94
Donati, J., Morin, J., Petit, P., et al. 2008, MNRAS, 390, 545
Donati, J.-F., Hébrard, E., Hussain, G., et al. 2014, MNRAS, 444, 3220
Gadun, A. S., & Pavlenko, Y. V. 1997, A&A, 324, 281
Gomes da Silva, J., Santos, N. C., Bonfils, X., et al. 2011, A&A, 534, A30
Hallinan, G., Littlefair, S., Cotter, G., et al. 2015, Natur, 523, 568
Horne, K. D. 1986, PASP, 98, 609
Jenkins, J. S., Ramsey, L. W., Jones, H. R. A., et al. 2009, ApJ, 704, 975
Kaltenegger, L., & Traub, W. A. 2009, ApJ, 698, 519
Knutson, H. A., Madhusudhan, N., Cowan, N. B., et al. 2011, ApJ, 735, 27
Kupka, F., Piskunov, N., Ryabchikova, T. A., Stempels, H. C., & Weiss, W. W. 1999, A&AS, 138, 119
Lohr, M. E., Norton, A. J., Anderson, D. R., et al. 2014, A&A, 566, A128
Mahadevan, S., Ramsey, L., Wright, J., et al. 2010, Proc. SPIE, 7735, 6
Marsden, S. C., Donati, J.-F., Semel, M., Petit, P., & Carter, B. D. 2006, MNRAS, 370, 468
Martín, E. L., Guenther, E., Zapatero Osorio, M. R., Bouy, H., & Wainscoat, R. 2006, ApJL, 644, L75
Mohanty, S., & Basri, G. 2003, ApJ, 583, 451
Montes, D., López-Santiago, J., Gálvez, M. C., et al. 2001, MNRAS, 328, 45
Morin, J., Donati, J., Petit, P., et al. 2008a, MNRAS, 390, 567
Morin, J., Donati, J.-F., Forveille, T., et al. 2008b, MNRAS, 384, 77
Morin, J., Donati, J.-F., Petit, P., et al. 2010, MNRAS, 407, 2269
Pavlenko, Y. V. 2014, ARep, 58, 825
Pavlenko, Y. V., Jones, H. R. A., Martín, E. L., et al. 2007, MNRAS, 380, 1285
Pavlenko, Y. V., & Schmidt, M. 2015, KPCB, 31, 90
Phan-Bao, N., Lim, J., Donati, J.-F., Johns-Krull, C. M., & Martín, E. L. 2009, ApJ, 704, 1721
Piskunov, N. E., Kupka, F., Ryabchikova, T. A., Weiss, W. W., & Jeffery, C. S. 1995, A&AS, 112, 525
Quirrenbach, A., Amado, P. J., Mandel, H., et al. 2010, Proc. SPIE, 7735, 13
Reid, I. N., & Hawley, S. L. 2005, New Light on Dark Stars: Red Dwarfs, Low-mass Stars, Brown Dwarfs (Berlin: Springer)
Reiners, A., & Basri, G. 2007, ApJ, 656, 1121
Reiners, A., & Basri, G. 2009, A&A, 496, 787
Reiners, A., & Basri, G. 2010, ApJ, 710, 924
Ribas, I. 2003, A&A, 400, 297

Rice, J. B., Wehlau, W. H., & Khokhlova, V. L. 1989, A&A, 208, 179
Rockenfeller, B., Bailer-Jones, C. A. L., & Mundt, R. 2006, A&A, 448, 1111
Ryabchikova, T. A., Pakhomov, Y. V., & Piskunov, N. E. 2011, KIzKU, 153, 61
Stassun, K. G., Kratter, K. M., Scholz, A., & Dupuy, T. J. 2012, ApJ, 756, 47
Thibault, S., Rabou, P., Donati, J.-F., et al. 2012, Proc. SPIE, 8446, 30
Tuomi, M., Jones, H. R. A., Barnes, J. R., Anglada-Escudé, G., & Jenkins, J. S. 2014, MNRAS, 441, 1545
Unruh, Y. C., & Collier Cameron, A. 1995, MNRAS, 273, 1
Williams, P. K. G., Berger, E., Irwin, J., Berta-Thompson, Z. K., & Charbonneau, D. 2015, ApJ, 799, 192
Zerbi, F. M., Bouchy, F., Fynbo, J., et al. 2014, Proc. SPIE, 9147, 23